Stratospheric Sudden Warmings as Self-Tuning Resonances. Part II: Vortex Displacement Events

J. G. ESLER AND N. JOSS MATTHEWMAN

Department of Mathematics, University College London, London, United Kingdom

(Manuscript received 17 December 2010, in final form 30 April 2011)

ABSTRACT

Vortex displacement stratospheric sudden warmings (SSWs) are studied in an idealized model of a quasi-geostrophic columnar vortex in an anelastic atmosphere. Motivated by the fact that observed events occur at a fixed orientation to the earth's surface and have a strongly baroclinic vertical structure, vortex Rossby waves are forced by a stationary topographic forcing designed to minimize excursions of the vortex from its initial position. Variations in the background stratospheric ''climate'' are represented by means of an additional flow in solid body rotation. The vortex response is determined numerically as a function of the forcing strength M and the background flow strength Ω.

At moderate M it is found that a large response, with many features resembling observed displacement SSWs, occurs only for a narrow range of Ω. Linear analysis reveals that for this range of Ω the first baroclinic azimuthal wave-1 Rossby wave mode is close to being resonantly excited. A forced nonlinear oscillator equation is proposed to describe the nonlinear behavior, and a method for determining the relevant coefficients numerically, using unforced calculations of steadily propagating vortex ''V states,'' is adopted. The nonlinear equation predicts some qualitative details of the variation in the response at finite M. However, it is concluded that strongly nonlinear processes, such as wave breaking and filament formation, are necessarily quantitatively important in determining the amplitude of the near-resonant response at finite M.

1. Introduction

Major midwinter stratospheric sudden warmings (SSWs) are defined to occur when there is a reversal of the usual westerly zonal mean winds at 60°N and 10 hPa, followed by their subsequent recovery. The topological evolution of the polar vortex during SSWs varies considerably between displacement events, where the vortex at a given level is observed to be displaced off the pole, and splitting events during which the vortex divides in two. The observational classification of Charlton and Polvani (2007) revealed that approximately 15 vortex displacement SSWs occurred in the Northern Hemisphere during 1957–2002 compared to 14 splitting events. Hence, each type of event spontaneously occurs approximately once every three years. Observed displacement events have recently been shown to exhibit two interesting features (Matthewman et al. 2009, see their Figs. 7–9):

(i) Vortex displacement SSWs are strongly baroclinic events with the displacement of the lower vortex typically opposite in sense to the upper vortex.
(ii) The sense of the vortex displacement at each level is generally fixed relative to the earth's surface.

Dynamical studies have primarily attributed the cause of SSWs to Rossby waves emanating from the troposphere, following the pioneering mechanistic model experiments of Matsuno (1971). Tung and Lindzen (1979) subsequently argued that, for a given stationary (Rossby wave) forcing, a large SSW-like response will result only if a linear free-traveling Rossby wave mode of the stratospheric flow is resonantly excited. Evidence that resonance played a role in a model study of the splitting SSW of 1979 has been given by Smith (1989), who used a quasi-linear[1] wave-mean flow model to show that the free-traveling wave 2 in

---

Corresponding author address: Gavin Esler, Department of Mathematics, University College London, 25 Gower Street, London WC1E 6BT, United Kingdom.
E-mail: gavin@math.ucl.ac.uk

[1] The weakly nonlinear analysis of Matthewman and Esler (2011) shows that to correctly capture the leading-order nonlinear aspects of wave-2 Rossby wave disturbances to a vortex, both mean flow and second harmonic terms must be considered, strongly suggesting that the quasi-linear model approach of Smith (1989) is not quantitatively accurate for investigation of the *nonlinear* aspects of resonance.

DOI: 10.1175/JAS-D-11-08.1

a primitive equation model approaches linear resonance toward the onset of the SSW. Here, the aim is to explore the relevance of the resonant excitation theory for the specific case of vortex displacement SSWs. The modeling philosophy will follow that of previous works on vortex splitting SSWs (Esler and Scott 2005; Esler et al. 2006), including the companion paper (Matthewman and Esler 2011, hereafter Part I). The idea is to select a model of the polar vortex that is sufficiently simple to facilitate analysis of the linear problem but that nevertheless retains sufficient complexity to capture realistic nonlinear behavior, including the observed baroclinic development and subsequent Rossby wave breaking. The following question can then be addressed: does nonlinear vortex development resembling observed SSWs result from resonant excitation of a free-traveling Rossby wave mode?

Most previous idealized studies of forced vortex Rossby waves in simple models allowing vertical propagation (e.g., Dritschel and Saravanan 1994; Waugh and Dritschel 1999; Wang and Fyfe 2000; Polvani and Saravanan 2000) did not focus on the issue of resonance, but they nevertheless uncovered behavior that has proved robust across different models. The response of a (effectively semi-infinite) vortex to forcing almost invariably results in strongly nonlinear wave breaking aloft, and it can result in the complete destruction of the vortex at upper levels (e.g., Fig. 5 of Polvani and Saravanan 2000). Superficially such Rossby wave breaking resembles that observed during SSWs. However, it is notable that although zonal mean winds are decelerated aloft, the total stratospheric angular momentum change recorded in the above studies (e.g., Fig. 6 of Polvani and Saravanan 2000) is typically much less than that observed during an SSW. At the lower levels that contribute the majority of the stratospheric angular momentum, the zonal winds remain relatively unchanged. Esler and Scott (2005) showed explicitly that off-resonant wave-2 forcing can lead to the upper-level wave breaking reported in the studies above, but only forcing that resonantly excited the gravest wave-2 vortex Rossby wave mode (the ''barotropic'' mode) can lead to a vortex split. It is natural to ask the question whether or not a similar result holds for vortex displacement SSWs. The resonantly excited mode in the displacement case must be a baroclinic mode, since the gravest wave-1 barotropic mode corresponds to a simple displacement of the entire vortex, a dynamically reversible process corresponding to a uniform translation of the entire (model) potential vorticity (PV) distribution.[2] Observed vortex displacement SSWs do not resemble uniform translations of the vortex.

Questions concerning the nonlinear dynamics of the model response to forcing are also of interest. Plumb (1981) extended the Tung and Lindzen (1979) linear analysis of vertical Rossby wave propagation in a β channel to include leading-order nonlinear effects. Leading-order nonlinearity arises from the variation in the angular frequency of vortex Rossby waves with their amplitude. In Part I a theory similar to Plumb's is developed to investigate vortex splits in a single-layer model of the polar vortex. The angular frequencies of nonlinear vortex Rossby waves are shown to have a significant dependence on amplitude. Further, a bifurcation is associated with this dependency, in which a small change in the model parameters can lead to an abrupt change in the maximum amplitude attained by the vortex Rossby waves as the vortex undergoes a nonlinear oscillation. The bifurcation can be clearly identified as the cause of vortex splitting SSWs in the simple model. Provided that the question in the second paragraph can be answered in the affirmative, the results of Part I prompt the following related questions relating to the specific nature of the nonlinearity in vortex displacement SSWs:

(i) What is the role of the leading (quadratic in wave amplitude) correction to the Rossby wave phase speed of the relevant baroclinic mode for the nonlinear dynamics? The success of the simple model equations used in Part I to predict the vortex response depends on the leading Rossby wave phase speed correction dominating over other nonlinear effects over a wide range of wave amplitudes.
(ii) Does the nonlinear oscillator equation [Eq. (31) in Part I; see also, e.g., Nayfeh and Mook 1979] give good quantitative predictions of the vortex response to moderate forcings?
(iii) What is the impact of ''strong'' nonlinearities, such as the wave breaking and ejection of filaments of vortex air reported in the above studies?

In section 2, the idealized quasigeostrophic model of a polar vortex in an anelastic atmosphere on an *f* plane is described in detail, including its numerical implementation. The linear theory of both forced and unforced vortex Rossby waves is revisited and generalized and a nonlinear oscillator equation is proposed to describe the nonlinear behavior. Section 3 describes the results from the full nonlinear model. The extent to which the dynamical evolution during particular experiments resembles that during observed SSWs is examined in detail, and the extent to which linear and nonlinear predictions of the disturbance amplitudes are qualitatively and quantitatively accurate is discussed. In section 4 conclusions are drawn.

---

[2] Much of the angular momentum change in the Polvani and Saravanan (2000) experiments discussed above appears to be barotropic and may therefore be primarily due to a uniform displacement of the vortex.

2. A model of vortex displacement SSWs

a. Model description and parameters

The equations describing the quasigeostrophic motion of fluid in an anelastic atmosphere on an *f* plane (e.g., Pedlosky 1987) are

$$[\partial_t + (\mathbf{u}\cdot\nabla_H)]q = 0,$$
$$\nabla_H^2\psi + \frac{1}{\rho}\left(\rho\frac{f_0^2}{N^2}\psi_z\right)_z = q,$$
$$\mathbf{u} = -\nabla\times\psi\mathbf{k}. \qquad (1)$$

Here $q(\mathbf{x}, t)$ is the quasigeostrophic PV, $\psi(\mathbf{x}, t)$ is the horizontal streamfunction, and $\mathbf{u}(\mathbf{x}, t)$ is the horizontal velocity. The vector $\mathbf{k}$ is the vertical unit vector and ∇_H^2 is the horizontal Laplacian. The density $\rho(z)$ is a monotonically decaying function of log-pressure height z, which for the special case of an isothermal stratosphere to be examined here becomes an exponential function $\exp(-z/H)$ with density scale height H. The buoyancy frequency N and Coriolis parameter f_0 determine the stratification and rotation rate, respectively.

The system (1) is subject to the following boundary condition (e.g., Held et al. 1995) at a solid near-horizontal lower boundary with topography $z = h_m(\mathbf{x})$:

$$[\partial_t + (\mathbf{u}\cdot\nabla_H)]\left(\psi_z - \frac{\kappa}{H}\psi + \frac{N^2}{f_0}h_m\right) = 0, \quad \text{on} \quad z = 0. \qquad (2)$$

Physically Eq. (2) corresponds to parcelwise conservation of potential temperature on the lower boundary. If the initial condition is such that the potential temperature [i.e., the advected quantity in Eq. (2)] is zero everywhere on the boundary at $t = 0$, the condition simplifies to

$$\psi_z - \frac{\kappa}{H}\psi + \frac{N^2}{f_0}h_m = 0 \quad \text{on} \quad z = 0, \qquad (3)$$

where $\kappa = 0.288$ is the ratio of the gas constant of air to its specific heat at constant pressure. Note that previous works (Waugh and Dritschel 1999; Esler and Scott 2005) have used an ersatz lower boundary condition of uniform temperature on the lower boundary [i.e., a lower boundary condition where the ψ term in Eq. (3) is omitted]. The effect of changing to the correct boundary condition here will be discussed below. Further conditions $\psi \to 0$ as $z \to \infty$ and $\psi \to 0$ as $|\mathbf{x}| \to \infty$ ensure decay of perturbations at high altitudes and large radial distances.

The stratospheric "climate" in the model is varied by adjusting the magnitude of a solid body rotation flow with streamfunction $\Psi = (1/2)\Omega_b r^2$. The flow equates to an additional uniform PV field $Q = 2\Omega_b$ throughout the domain and is therefore dynamically passive.

Following Scott and Dritschel (2005), Eq. (1) is nondimensionalized using the scale height H as the vertical length unit and the "scale height Rossby radius" $L_R = NH/f_0$ as the horizontal length scale; PV is scaled by a typical vortex PV anomaly Δ_0, time by Δ_0^{-1}, horizontal velocities by $\Delta_0 L_R$, and the streamfunction by $\Delta_0 L_R^2$. The topography is nondimensionalized by writing $h_m = H_m h(\mathbf{x})$, where H_m is a representative height and $h(\mathbf{x})$ a dimensionless function. Replacing dimensional variables by their nondimensional counterparts where appropriate from here onward, and including the additional background rotation flow, the equations and boundary conditions can be written in the following nondimensional form:

$$[\partial_t - (\Omega y + \psi_y)\partial_x + (\Omega x + \psi_x)\partial_y](\nabla_H^2\psi + \psi_{zz} - \psi_z) = 0,$$
$$\psi_z - \kappa\psi = -Mh, \quad \text{on} \quad z = 0,$$
$$\psi \to 0, \quad \text{for} \quad z \to \infty. \qquad (4)$$

The nondimensional parameters (Ω, M) measuring the significance of the background flow and the strength of the topographic forcing, respectively, are defined by

$$\Omega = \frac{\Omega_b}{\Delta_0}, \quad M = \frac{H_m f_0}{H\Delta_0} \qquad (5)$$

and will control the outcome in the experiments described below.

The initial condition for each experiment is an isolated vortex with excess PV profile:

$$\nabla_H^2\psi + \psi_{zz} - \psi_z = \begin{cases} \Delta(z) & \text{for} \quad r < R(z), \quad z_b < z < z_t, \\ 0 & \text{otherwise.} \end{cases} \qquad (6)$$

The dynamics is subsequently controlled by advection of the vortex boundary [i.e., the boundary of the high PV region; it is assumed that $\Delta(z) > 0$ throughout $z_b < z < z_t$]. To fix the definitions of Δ_0 and $\Delta(z)$, the normalization condition

$$\int_{z_b}^{z_t} e^{-z}\Delta(z)R(z)^2\,dz = \int_{z_b}^{z_t} e^{-z}R(z)^2\,dz = \mathcal{M}$$

is imposed on $\Delta(z)$. The quantity $\mathcal{M}$ is the vortex mass.

Table 1 gives a list of suitable choices for dimensions and parameters, referred to as the dimensionalization STANDARD below, that can be used for comparison between model quantities and stratospheric parameters. The values are largely those used by Waugh and Dritschel

TABLE 1. Detailing the model dimensions and dimensionalization STANDARD used throughout.

Quantity	Scale in model	STANDARD dimensionalization	Notes
Vertical length	H	6.14 km	Scale height $H = RT_s/g$ ($R = 287.06$ m^2 s^{-2} K^{-1} is gas constant for air; $T_s = 210$ K is isothermal stratosphere temperature; $g = 9.81$ m s^{-2} is gravitational acceleration)
Horizontal length	L_R	900 km	Rossby radius $L_R = NH/f_0$ ($N = 0.0214$ s^{-1} is buoyancy frequency; $N^2 = g^2/c_pT_s$, where $c_p = 1000$ m^2 s^{-2} K^{-1} is specific heat at constant pressure of air; $f_0 = 1.454 \times 10^{-4}$ s^{-1} is Coriolis parameter)
Time	Δ_0^{-1}	$1/4\pi$ days	$\Delta_0 = f_0$ scaling choice
Horizontal velocity	$\Delta_0 L_R$	130.9 m s^{-1}	
Streamfunction	$\Delta_0 L_R{}^2$	5.798×10^4 m^2 s^{-1}	

(1999) except that a larger value of Δ_0 is chosen. The new value is necessary to obtain realistic stratospheric winds in the experiments below, as a vortex of finite height located between levels $z = z_b$ and $z = z_t$ above the lower boundary is used, as opposed to a vertically uniform semi-infinite vortex in $z \geq 0$. The present value $\Delta_0 = f_0$ is consistent with observations (e.g., Fig. 2 of Matthewman et al. 2009) but is at the outer limit of the validity of the quasigeostrophic theory, which is formally valid for $\Delta_0 \ll f_0$.

b. Linear theory of forced vortex Rossby waves

In this section the linear theory of unforced and forced vortex Rossby waves is reconsidered. Waugh and Dritschel (1999) considered the general linear problem for arbitrary vortex radius $R(z)$ and PV profile $\Delta(z)$ but discretized the problem at an early stage, rendering the mathematical structure of the problem opaque. Although the continuum limit has been considered for certain special cases (Wang and Fyfe 2000; Esler and Scott 2005), to our knowledge there has been no general treatment.

Linear theory follows from consideration of disturbances to the vortex boundary that are small in the sense to be discussed below. First, note that the streamfunction for any arbitrary disturbance to the columnar vortex can be expressed as a Green's function integral (see appendix A):

$$\begin{aligned}\psi(\mathbf{x}, z) &= \int_{z_b}^{z_t}\int_{\mathcal{S}} G(|\mathbf{x} - \mathbf{x}'|, z|z')q(\mathbf{x}', z')\, d^2\mathbf{x}'\, dz', \\ &= \int_{z_b}^{z_t} \Delta(z')\int_{\mathcal{D}(z')} G(|\mathbf{x} - \mathbf{x}'|, z|z')\, d^2\mathbf{x}'\, dz', \qquad (7)\end{aligned}$$

where $\mathcal{S}$ denotes the horizontal plane and $\mathcal{D}(z')$ denotes the area occupied by the vortex at level z'. Taking $-\nabla \times \psi\mathbf{k}$ and applying Green's theorem in the plane at every level results in an expression for the velocity

$$\mathbf{u}(\mathbf{x}, z) = -\int_{z_b}^{z_t} \Delta(z')\oint_{\partial\mathcal{D}(z')} G(|\mathbf{x} - \mathbf{x}'|, z|z')\, d\mathbf{x}'\, dz' \qquad (8)$$

where the inner path integral is around $\partial\mathcal{D}(z')$, the boundary of $\mathcal{D}(z')$.

Next, linearity is introduced by taking the vortex boundary to be located at

$$\mathbf{x}'(\theta, z', t) = [R(z') + \epsilon\eta(\theta, z', t)]\hat{\mathbf{r}}(\theta), \quad 0 \leq \theta < 2\pi,$$

where $\hat{\mathbf{r}}(\theta)$ and $\hat{\boldsymbol{\theta}}(\theta)$ denote the radial and azimuthal unit vectors in cylindrical polar coordinates (r, θ, z); it is taken that $\epsilon \ll 1$ and $|\eta_\theta|$, the magnitude of the azimuthal gradient of η, is of order unity. The next step is to use the expression (8) for $\mathbf{u}$ in the kinematic condition for the vortex edge

$$\epsilon(\eta_t + \Omega\eta_\theta) = (\mathbf{u} \cdot \mathbf{n})_c, \qquad (9)$$

where $\mathbf{n}$ is the (horizontal) normal vector given by

$$\mathbf{n}(\theta, z) = \hat{\mathbf{r}} - \frac{\epsilon\eta_\theta}{(R + \epsilon\eta)}\hat{\boldsymbol{\theta}}, \qquad (10)$$

and the subscript c denotes evaluation on the contour. Linearizing the expression for $(\mathbf{u} \cdot \mathbf{n})_c$, which following the analogous steps in Part I [see their Eqs. (12), (13), and (A2)–(A5)] results in

$$(\mathbf{u} \cdot \mathbf{n})_c(\theta, z, t) = \epsilon\mathcal{L}\eta_\theta + O(\epsilon^2), \qquad (11)$$

where $\mathcal{L}$ denotes the linear operator defined for a general function $f(\theta, z)$ to be

$$\mathcal{L}f(\theta, z) = \frac{1}{R(z)}\int_{z_b}^{z_t}\int_0^{2\pi} \Delta(z')R(z')G[R(\tilde{\theta}, z, z'), z|z'][f(\theta, z)\cos\tilde{\theta} - f(\theta + \tilde{\theta}, z')]\, d\tilde{\theta}\, dz',$$

where

$$\mathcal{R}(\tilde{\theta}, z, z') = [R(z)^2 + R(z')^2 - 2R(z)R(z')\cos\tilde{\theta}]^{1/2}.$$

The linearized kinematic condition at the vortex edge can thus be written

$$\eta_t + \Omega\eta_\theta = \mathcal{L}\eta_\theta. \qquad (12)$$

Equation (12) is an integro-differential equation describing the evolution in time of a general disturbance $\eta(\theta, z, t)$. It can be simplified if the evolution of a disturbance consisting of a single azimuthal wavenumber is considered

$$\eta(\theta, z, t) = \mathrm{Re}\,\hat{\eta}^k(z, t)e^{ik\theta}. \qquad (13)$$

Inserting the above ansatz (13) into Eq. (12), using the expression (A2) for G in the integral, and using the Neumann addition formula [Watson 1944, see ch. 11, Eq. (8)] to expand the modified Bessel function terms as

$$K_0[(a^2 + b^2 - 2ab\cos\tilde{\theta})^{1/2}] = I_0(a)K_0(b) + 2\sum_{n=1}^{\infty} I_n(a)K_n(b)\cos n\tilde{\theta} \quad (a \le b),$$

results in the following integro-differential evolution equation:

$$\hat{\eta}^k_t + ik[\Omega + \Omega_c(z)]\hat{\eta}^k = ik\int_{z_b}^{z_t} S^k(z, z')\hat{\eta}^k(z')\,dz', \qquad (14)$$

with the "self-induced" angular velocity Ω_c given by

$$\Omega_c(z) = \int_{z_b}^{z_t} S^1(z, z')\,dz',$$

and the integral kernel S^k given by

$$S^k(z, z') = \frac{(1 - 2\kappa)\Delta(z')R(z')e^{\kappa z - (1-\kappa)z'}}{R(z)} I_k(\gamma_0 R_-)K_k(\gamma_0 R_+) + \frac{2\Delta(z')R(z')e^{(z-z')/2}}{\pi R(z)} \times \int_0^{\infty} I_k[\gamma(m)R_-]K_k[\gamma(m)R_+]\cos[mz' + \vartheta(m)]\cos[mz + \vartheta(m)]\,dm,$$

where

$$R_+(z, z') = \max[R(z), R(z')],$$
$$R_-(z, z') = \min[R(z), R(z')],$$
$$\gamma_0 = \sqrt{\kappa(1 - \kappa)},$$
$$\gamma(m) = m^2 + \frac{1}{4}, \quad \text{and}$$
$$\vartheta(m) = \tan^{-1}\left(\frac{1 - 2\kappa}{2m}\right).$$

Despite its somewhat complicated appearance, for typical well-behaved $R(z)$ and $\Delta(z)$ the integral kernel $S^k(z, z')$ is a relatively benign continuous function of its two arguments, except for an integrable (logarithmic) singularity at $z = z'$, typical of Green's function kernels appearing in vorticity dynamics. Note that $S^k(z, z')$ can be interpreted as a measure of the influence of the wavenumber k Rossby wave at level z' on the development of the wavenumber k Rossby wave at level z within the vortex, account being taken of the lower boundary.

If solutions of Eq. (14) are sought of the form

$$\hat{\eta}^k(z, t) = Z(z)e^{-i\omega t}, \qquad (15)$$

the result is the following eigenvalue problem for ω/k:

$$\mathcal{L}^k Z \equiv \int_{z_b}^{z_t} S^k(z, z')Z(z')\,dz' - [\Omega + \Omega_c(z)]Z(z) = -\frac{\omega}{k}Z. \qquad (16)$$

Equation (16) is a linear homogeneous Fredholm equation of the third kind (e.g., Porter and Stirling 1990). It is well known that a third-kind Fredholm equation such as Eq. (16) can be transformed into the more familiar second-kind equations provided that (in this case) $\omega/k - \Omega - \Omega_c(z) \neq 0$ for $z \in [z_b, z_t]$. Different behavior can therefore be expected for eigenvalues in the range

$$\min_z[\Omega + \Omega_c(z)] < \frac{\omega}{k} < \max_z[\Omega + \Omega_c(z)], \qquad (17)$$

as opposed to outside this range. Equation (16) can be readily discretized on a grid of N points $[z_i = z_b + (i - 1/2)(z_t - z_b)/N,\ i = 1, \ldots, N]$ and solved using a standard numerical eigenvalue routine, recovering essentially the discrete problem examined by Waugh and Dritschel (1999, see section 4a). Repeated solution over a range of values of N reveals that normal mode solutions, associated with discrete eigenvalues, have ω/k outside the range (17), whereas within the range (17) results converge toward a continuous spectrum of eigenvalues as $N \to \infty$. An example calculation is discussed in section 3a below. Physically there is a clear explanation for the different behaviors: normal modes do not have critical levels within the vortex (where ω/k equals the rotation rate of the vortex at the vortex edge), whereas critical levels exist for the continuous range of phase speeds within expression (17).

An important special case of a normal mode eigenfunction solution of Eq. (16) occurs for $k = 1$. The eigenfunction $Z(z)$ = constant can be seen to be an exact solution of Eq. (16) corresponding to the angular frequency eigenvalue $\omega/k = \Omega$. This is the pure displacement mode corresponding to a uniform displacement of the entire vortex from the pole. The dynamics associated with the pure displacement mode are essentially trivial and are entirely reversible. There is no nonlinearity associated with the mode and its role in vortex displacement SSWs will be argued below to be of secondary importance. A further property of the eigenvalue Eq. (16) is that the frequency ω of each mode varies linearly with $\Omega(\sim\Omega k)$. The background rotation parameter Ω can therefore be used to bring each mode into linear resonance, and it plays essentially the same role as in the corresponding analysis in Part I.

One key property of the linear operator $\mathcal{L}^k$, which follows directly from the symmetry relation

$$S^k(z,z')\Delta(z)R(z)^2e^{-z} = S^k(z',z)\Delta(z')R(z')^2e^{-z'},$$

is that it is Hermitian with respect to an inner product defined for complex valued functions $f(z)$ and $g(z)$ on $[z_b, z_t]$ to be

$$\langle f,g\rangle = \int_{z_b}^{z_t} e^{-z}\Delta(z)R(z)^2f(z)g^*(z)\,dz, \qquad (18)$$

where the superscript asterisk denotes complex conjugate. That is,

$$\langle\mathcal{L}^kf,g\rangle = \langle f,\mathcal{L}^kg\rangle^*. \qquad (19)$$

It follows (cf. Sturm–Liouville theory) that eigenfunctions $Z_a(z)$, $Z_b(z)$ associated with distinct eigenvalues ω_a, ω_b are orthogonal with respect to the inner product, such that

$$\langle Z_a,Z_b\rangle = 0, \quad (a \neq b). \qquad (20)$$

Henceforth all such eigenfunctions $Z_a(z)$ will be assumed normalized so that $\langle Z_a,Z_a\rangle = \mathcal{M}$.

The inner product is an angular pseudomomentum norm, where angular pseudomomentum is defined (following Dritschel and Saravanan 1994) to be

$$\mathcal{A} = \mathcal{J}_t - \mathcal{J}_0, \quad \text{where}$$
$$\mathcal{J}_t = \frac{1}{2}\int_{z_b}^{z_t}\int_D e^{-z}r^2q(\mathbf{x},t)\,d^2\mathbf{x}\,dz \qquad (21)$$

is the vortex angular impulse and $\mathcal{J}_0$ is its value for the undisturbed vortex. For a single-wavenumber disturbance consisting of a linear combination of n discrete normal modes[3]

$$\eta(\theta,z,t) = \mathrm{Re}\sum_{j=1}^{n}\epsilon A_j^k(t)Z_j^k(z)\exp(ik\theta), \qquad (22)$$

expansion of the explicit expression for $\mathcal{A}$ [e.g., Eq. (14) of Esler and Scott 2005] and use of the orthogonality condition [Eq. (20)] reveals that

$$\mathcal{A} = \epsilon^2\frac{\pi}{2}\mathcal{M}\sum_{j=1}^{n}|A_j^k|^2 + O(\epsilon^3); \qquad (23)$$

that is, each linear mode makes an independent contribution to $\mathcal{A}$ that is quadratic in its amplitude.

The above analysis indicates that the natural framework to analyze the forced problem is in terms of the projection of the disturbances onto the relevant vertical eigenfunctions, and the natural quadratic norm for wave amplitude is $\mathcal{A}$. The forcing enters the problem through the topography distribution $h(\mathbf{x})$ appearing in the lower boundary condition. As in the single-layer model of Part I, the effect of the nonhomogeneous lower boundary condition in the system (4) is equivalent to including an additional advecting "forcing velocity" $\mathbf{u}_M$ in the unforced problem, defined here by

$$\begin{aligned}\mathbf{u}_M &= -\nabla\times\psi_M\mathbf{k},\\ \nabla_H^2\psi_M + \psi_{Mzz} - \psi_{Mz} &= 0,\\ \psi_{Mz} - \kappa\psi_M &= -Mh \quad z = 0,\\ \psi_M &\to 0 \quad z\to\infty.\end{aligned} \qquad (24)$$

Exploiting the above equivalence, the integro-differential Eq. (12) in the presence of forcing becomes, in cylindrical coordinates,

$$\begin{aligned}\eta_t + (\Omega - \mathcal{L})\eta_\theta &= F_\theta,\\ F(\theta,z) = \mathrm{Re}\sum_{k=1}^{\infty}\hat{F}^ke^{ik\theta} &= -\frac{\psi_M[R(z),\theta,z]}{R(z)}.\end{aligned} \qquad (25)$$

The forcing F in Eq. (25) is simply the radial component of the velocity due to the forcing evaluated at the vortex boundary. Inserting the ansatz (22) into Eq. (25), setting

---

[3] Note that to express a general disturbance in terms of the eigenfunctions of Eq. (16), both a sum over all wavenumbers k and, for each k, an integral over the continuous spectrum in addition to a sum over all discrete normal modes is required.

$\epsilon = M \ll 1$, and then taking the inner product with each vertical eigenfunction reveals that the complex amplitude A_j^k of a linear mode with frequency $\omega_{0(k,j)}$ and vertical structure function $Z_j^k(z)$ evolves according to

$$\frac{dA_j^k}{dt} + i\omega_{0(k,j)}A_j^k = iF_j^k, \quad \text{where} \quad F_j^k = k\langle Z_j^k, \hat{F}^k\rangle. \tag{26}$$

The linear amplitude Eq. (26) is analogous to the linear evolution Eq. (17) of Part I, with the forcing F_j^k given by the projection of F onto the relevant azimuthal and vertical eigenfunction. Understanding how a given $h(\mathbf{x})$ generates a forcing function $F(\theta, z)$, and how the vertical structure of F projects onto that of the eigenfunctions is key to the linear problem.

c. *A weakly nonlinear model equation*

There is clearly a close relationship between the linear problem described above and the single layer case described in Part I. There is no obstacle, in principle, to extending the weakly nonlinear analysis given in Part I to the three-dimensional system considered here. The typical weakly nonlinear scenario occurs when a single discrete eigenmode, with indices (k, j), is near-resonantly excited. The eigenfrequency of this mode must therefore be close to zero and can therefore be written $\omega_{0(k,j)} = M^{2/3}\tilde{\omega}_{0(k,j)}$ (under the assumption that $M \ll 1$). Following the analysis in Part I, the amplitude of the near-resonantly excited mode will scale with $M^{1/3}$ and the disturbance at leading order can be written

$$\eta(\theta, z, t) = \mathrm{Re}\,\epsilon A_j^k(T)Z_j^k(z)e^{ik\theta},$$

where $\epsilon = M^{1/3}$ and T is a rescaled long time variable $T = \epsilon^2 t$. All other eigenfunctions have amplitudes $O(M = \epsilon^3)$. Following the analysis of Part I, $A_j^k(T)$ will evolve according to

$$\frac{dA_j^k}{dT} + i\tilde{\omega}_{0(k,j)}A_j^k + i\omega_{2(k,j)}A_j^k|A_j^k|^2 = iF_j^k, \tag{27}$$

where the nonlinear coefficient $\omega_{2(k,j)}$ is determined from the details of the nonlinear expansion of the velocity field.

Given its lengthy character, however, an explicit calculation of $\omega_{2(k,j)}$ will not be pursued here. Instead, the value of $\omega_{2(k,j)}$ will be estimated from nonlinear calculations of the unforced problem. The frequencies of V-state solutions, meaning steadily propagating nonlinear vortex Rossby waves (e.g., Polvani et al. 1989) or equivalently steadily rotating disturbed vortices, can be estimated from Eq. (27). If a V state has constant wave amplitude $\epsilon|A_j^k|$, the nonlinear Eq. (27) indicates that it must propagate with angular frequency

$$\omega = \omega_{0(k,j)} + \epsilon^2|A_j^k|^2\omega_{2(k,j)} + O(\epsilon^3). \tag{28}$$

Equation (28) can be used to estimate $\omega_{2(k,j)}$ using calculations of the angular frequencies of a family of V states in which the fundamental $\epsilon|A_j^k|$ is varied, as will be described below.

Figure 1 summarizes results from the theory of nonlinear oscillators (e.g., Nayfeh and Mook 1979) covered in more detail in Part I. The schematic plot shows the peak response in the amplitude of the fundamental wave $\max_t[\epsilon|A_j^k(t)|]$ as a function of Ω, when M is fixed. For values of Ω far from the critical value for linear resonance $\Omega = \Omega_c$ (Ω_c is defined as the value of Ω for which linear frequency of the fundamental $\omega_{0(k,j)} = 0$), both the weakly nonlinear Eq. (27) and linear Eq. (26) predict an identical response. Qualitatively different behavior is predicted, however, as $\Omega \rightarrow \Omega_c$. The linear response is singular at Ω_c, but the nonlinear response remains finite and in fact peaks at $\Omega_{\mathrm{nl}} = \Omega_c - 3k^{-1}[\omega_{2(k,j)}M^2(F_j^k)^2/2]^{1/3}$, where the maximum amplitude attained is

$$\epsilon|A_j^k| = A_0 = [16MF_j^k/\omega_{2(k,j)}^2]^{1/3}. \tag{29}$$

The prediction (29) will be compared with numerical results from the full nonlinear model below.

d. *Numerical implementation of full nonlinear model*

The nonlinear numerical model used to solve the system (4) is essentially that of Macaskill et al. (2003) where full details are given. Briefly, the model employs the contour advective semi-Lagrangian (CASL) algorithm (Dritschel and Ambaum 1997), in which the PV advection step uses a contour representation for the PV field with contours then interpolated onto a regular grid for the inversion step. A grid of 96 radial × 192 azimuthal × 120 vertical points is used for the inversion step, with the radial points equally spaced in $s = r^{1/2}$. The equivalent resolution of the contoured PV corresponds to a horizontal grid of around 4 times the above density. Only a subset of the vertical levels, corresponding to $z_b < z < z_t$ are "active" in the sense that they contain vortex PV anomalies. Additional boundary conditions are employed, of no normal flow on the outer wall, $\psi_\theta = 0$ on $r = 30L_R$, and zero potential temperature anomaly on an upper lid $\psi_z - \kappa\psi = 0$ on $z = 12H$. Tests revealed that the outer wall and upper lid positions are sufficiently distant that the dynamics closely approximates that of the unbounded volume $\mathbf{x} \in \mathcal{S}, z > 0$ used in the analysis of sections 2a–c.

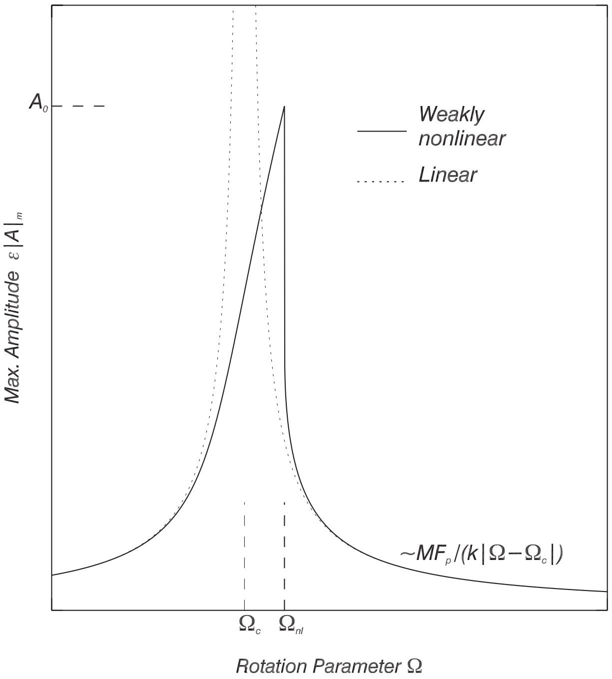

FIG. 1. Schematic illustrating the predictions for the maximum amplitude of the disturbance for the linear Eq. (26) (dotted curve) and the weakly nonlinear Eq. (27) (solid curve) for fixed M, as a function of Ω. The value of Ω leading to linear resonance is marked as Ω_c and the value leading to the maximum nonlinear response is marked as Ω_{nl}.

The main adaptation of the present model compared to that of Macaskill et al. (2003) is the use of the correct lower boundary condition in Eq. (4). The Sturm–Liouville procedure described in Macaskill et al. (2003, see section 2.2.2) was modified for the new boundary condition, resulting in a modified set of vertical eigenfunctions and eigenvalues for use in the PV inversion step.

The initial vortex is discretized at each level by representing the vortex edge by a single circular contour made up of discrete points or nodes. The initial node density is 51 nodes per contour, except where stated otherwise below. The model is then integrated forwards with a time step of $\delta t = 0.1\pi\Delta_0^{-1}$, with contour surgery performed on the PV contours at each time step to remove PV at scales below that of the fine horizontal grid.

3. Results: Nonlinear experiments and comparison with theory

In this section a parameter sweep of nonlinear model experiments will be described. Results will be interpreted using the linear and weakly nonlinear theories introduced in sections 2b and 2c.

a. Experimental setup

An identical initial PV distribution is used for each model experiment within the main parameter sweep. The initial flow is due to a cylindrical vortex with a vertical depth of four scale heights ($4H$), located between $z = H$ and $z = 5H$, as is consistent with observations prior to displacement SSWs (e.g., Fig. 2c of Matthewman et al. 2009), if the tropopause is identified with $z = 0$. The vortex radius profile (units of L_R) and PV jump profile (units of Δ_0) are given by [see Eq. (6)]

$$R(z) = 3 - \alpha\left[\frac{z - (1/2)(z_b + z_t)}{z_t - z_b}\right]^2,$$
$$\Delta(z) = 1, \quad z_b < z < z_t, \qquad (30)$$

where $\alpha = 4.8$. The position of the vortex edge is shown in Fig. 2a (thick curve). The parabolic profile is a rough fit to observations before displacement SSWs, although the value of α is chosen primarily to minimize the early onset of weak wave breaking at the top and bottom of the vortex. The initial vortex might therefore be considered "preconditioned" by prior wave-breaking events. Experiments performed with other values of α, while exhibiting slightly more complex behavior, nevertheless give similar results.

The stratospheric jet, or azimuthal mean winds $\overline{u}(r, z)$, associated with the initial vortex when $\Omega = 0$ is shown in Fig. 2a. The jet maximum (>90 m s^{-1} under the STANDARD dimensionalization given in Table 1) is located at a radius close to the vortex edge ($2.6L_R \approx 2300$ km from the pole) and four scale heights above the lower boundary (tropopause), and the flow overall is reminiscent of a strong midwinter stratospheric jet. It will be shown below, however, that SSW-like behavior occurs only when the jet in Fig. 2a is weakened by 25 m s^{-1} or so by the addition of the background rotation flow (i.e., $\Omega < 0$).

The three leading eigenfunctions for the azimuthal wavenumber-1 ($k = 1$) linear problem (again with $\Omega = 0$) are shown in Fig. 2b, and are denoted $Z_1^1(z)$, $Z_2^1(z)$, and $Z_3^1(z)$ in the notation introduced above. Note that $Z_1^1(z)$ is the vertically uniform "pure displacement mode" discussed above. The second eigenfunction $Z_2^1(z)$, to be referred to as the "first baroclinic eigenfunction" below, will be shown to play the dominant role in the dynamics of the forced experiments. The reason that $Z_3^1(z)$ and other possible modes, including the continuous spectrum, are not found to have a significant role is the nature of their excitation by the topographic forcing, to be discussed below. The corresponding eigenvalues [$\omega_{0(1,1)} = 0, \omega_{0(1,2)}, \omega_{0(1,3)}$] are illustrated in Fig. 2c. The calculation is repeated on discrete grids of varying resolution ($N = 40, 80, 120$) to ensure convergence, and all eigenvalues of the

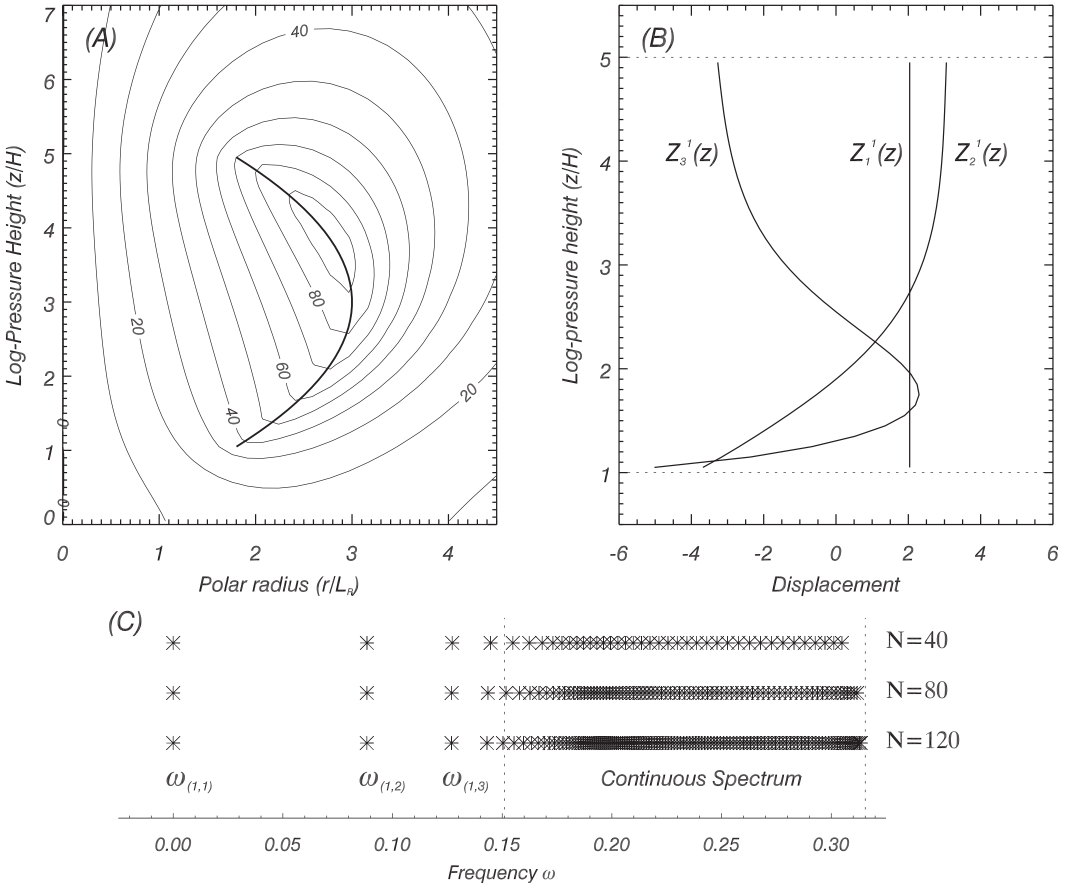

FIG. 2. (a) Initial zonal (azimuthal) mean wind $\overline{u}(r, z)$ for no solid body rotation ($\Omega = 0$). The contour interval is 10 m s^{-1} using the dimensionalization STANDARD. The vortex boundary used in the calculations is marked as a thick solid line. (b) The three leading eigenfunctions $Z_1^1(z)$, $Z_2^1(z)$, and $Z_3^1(z)$ of the $k = 1$ linear vortex Rossby wave Eq. (16), for the vortex plotted in (a). (c) The corresponding eigenvalue spectra, calculated on a discrete grid of $N =$ 40, 80, and 120 points, respectively. The first three eigenvalues are labeled, as is the continuous spectrum. The boundaries of the continuous spectrum, given by range (17), are marked with dotted lines.

discretized problem are shown in Fig. 2c. For the vortex in Fig. 2a the calculation appears to converge to give four discrete eigenvalues for $k = 1$, corresponding to four discrete normal modes. All other eigenvalues, within the range (17) delineated by the dotted lines, do not converge to fixed values with increasing N but instead fill out the continuous spectrum. The eigenfunctions of Eq. (16) within the continuous spectrum are singular at the critical level $z = z_c$ where the rotation rate of the vortex equals the rotation rate of the discrete "mode" $\Omega + \Omega_c(z_c) = \omega/k$.

An identical $h(\mathbf{x})$, shown in Fig. 3, is used in each model experiment. The topography represents the forcing effects of both surface topography and of stationary planetary Rossby waves at tropopause level. The view adopted here of the most consistent modeling choice for a mechanistic lower boundary forcing is as follows. The lower boundary condition should be chosen to match ψ_M throughout the stratosphere, because of the remote influence of the physical lower boundary and troposphere (i.e., all parts of the atmosphere not represented in the model), rather than to reflect the geopotential height or isentropic displacement at a particular level. The choice of the physical boundary condition (3) as opposed to specifying temperature (as in Waugh and Randel 1999; Esler and Scott 2005) or geopotential on the lower boundary is important in ensuring physically realistic decay rates with z for ψ_M. In particular, the correct lower boundary condition does not lead to ψ_M having a barotropic component, unlike the ersatz temperature boundary condition (Scott and Dritschel 2005).

For simplicity, $h(\mathbf{x})$ is given in polar coordinates by

$$h(r, \phi) = [J_1(\lambda_1 r) + \tilde{\alpha} J_1(\lambda_2 r)] \cos\phi. \qquad (31)$$

The functional form of the topography has been chosen to make it straightforward to solve Eq. (24) for the topographic streamfunction

$$\psi_M(r,\phi,z) = \left\{c_1 J_1(\lambda_1 r)\exp\left[-\left(\sqrt{\frac{1}{4}+\lambda_1^2}-\frac{1}{2}\right)z\right] + c_2\tilde{\alpha}J_1(\lambda_2 r)\exp\left[-\left(\sqrt{\frac{1}{4}+\lambda_2^2}-\frac{1}{2}\right)z\right]\right\}\cos\theta,$$

$$c_i = \frac{1}{\kappa + \sqrt{\frac{1}{4}+\lambda_i^2}-\frac{1}{2}}, \quad i = 1,2 \tag{32}$$

and thereby obtain F using Eq. (25). The possible values of λ_i are constrained by the need to satisfy the no-normal-flow condition on the outer boundary, which requires $30\lambda_i = j_{1m}$, where j_{1m} is a root of the Bessel function $J_1(r)$. The fifth and third roots are chosen, giving $\lambda_1 \approx 0.549$ and $\lambda_2 \approx 0.339$. The constant $\tilde{\alpha} = -0.7885$ is chosen, using a Newton-type iteration, so that $\langle Z_1^1, \hat{F}^1\rangle = 0$. In other words, the forcing is constrained so that the linear pure displacement mode (see section 2b) is not directly excited by the forcing. This is a key point in the experimental design. Since vortex displacement SSWs are strongly baroclinic, it is clear that excitation of the pure displacement mode does not play a key role in the dynamics, and since the displacement mode simply represents a shift in the vortex position relative to the surface it will at most contribute only to ''reversible'' dynamics. To design a clean set of experiments in which the focus is on the nonreversible baroclinic dynamics, it makes sense to minimize the excitation of the displacement mode throughout the experiment, so that the vortex remains over the model pole and thus experiences the same forcing velocity throughout. For the purposes of comparison with observations, the model pole (i.e., the origin) is best identified with the density-weighted vertically averaged centroid of the observed vortex, which lies slightly off the pole (e.g., Waugh and Randel 1999). The filtering of the topography ensures that the modeled vortex centroid, in common with the observed centroid during a displacement SSW, does not undergo a large excursion from its initial position. Tests confirmed that the above choice of $\tilde{\alpha}$ minimized migrations of the three-dimensional vortex centroid from the model pole throughout all experiments.

The level of excitation of other modes, such as the second baroclinic mode $Z_3^1(z)$, can be assessed in comparison with the excitation of the first baroclinic mode. Only large horizontal scales $\gtrsim L_R$ are present in $h(\mathbf{x})$ and, as a consequence of the inversion procedure (24), ψ_M thus decays slowly in the vertical and is a slowly varying function of z. Therefore, if a particular eigenfunction varies rapidly in the vertical (i.e., has many zeroes), the amplitude of the projection of the forcing function onto it will be small, and the level of its excitation will be weak. In the particular example given, and indeed for all physically plausible forcings $h(\mathbf{x})$, we find that

$$\langle \hat{F}^1, Z_2^1\rangle \gg \langle \hat{F}^1, Z_3^1\rangle$$

by an order of magnitude. Projections of $\hat{F}^1$ onto eigenfunctions within the continuous spectrum are also found to be comparably weak. The first baroclinic mode is therefore the only mode significantly excited by the forcing. It will therefore be the focus in all that follows.

The main parameter sweep consists of 72 experiments with parameters in the range $\Omega \in [-0.11, -0.0375]$ and $M \in [0, 0.5]$. All experiments are integrated for time $T = 160\pi\Delta_0^{-1} = 40$ days in the STANDARD dimensionalization. Results will be reported in section 3c below. Results from a set of unforced experiments will be considered next.

b. *Unforced experiments and vortex V states*

Figure 4 shows results from an unforced experiment with $(\Omega, M) = (-0.125, 0)$. In contrast to the forced experiments described above, the initial conditions for Fig. 4 are derived from the V-state algorithm described in appendix B. The left panel shows a three-dimensional view of a calculated V state constructed around the first baroclinic mode for azimuthal wavenumber 1 (see Fig. 2b for the corresponding vertical structure function $Z_2^1(z)$. The amplitude of the fundamental is set to $|A_2^1| = a = 0.4405$ (setting $\epsilon = 1$ without loss of generality) and the higher harmonics are then calculated as described in appendix B. The right panels show three snapshots of cross sections through the lower ($z = 2H$) and upper ($z = 4H$) vortex. The snapshots show clearly that the calculated V state is rotating uniformly.

The aim of the set of V-state experiments is to estimate the unknown nonlinear coefficient $\omega_{2(1,2)}$ for use in Eq. (27). The value of $\omega_{2(1,2)}$ is a measure of the rate of change of the fundamental wave frequency with the square of the vortex Rossby wave amplitude. The amplitude dependence of the wave propagation speed was shown in Part I to be the key nonlinear process for understanding the simple model of vortex splitting SSWs, and the aim here is to investigate if the same is true for displacement SSWs. Figure 5 shows the calculated frequencies ω for V states with three different fundamental amplitudes ($|A_2^1| = a = \{0.3524, 0.4405, 0.5286\}$), together with a cubic fit to $\omega(a)$ (solid curve). The fitting parameters can be used to obtain a numerical estimate of the linear

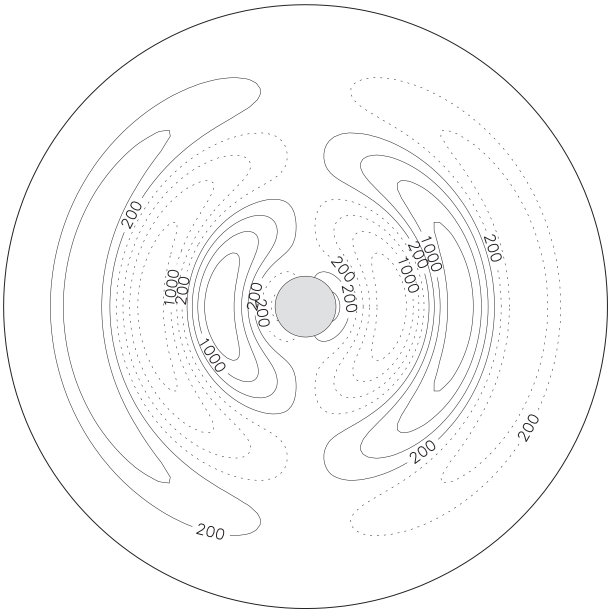

FIG. 3. The topographic forcing function $Mh_m(r, \phi)$ for $M = 0.5$ (the maximum value used in the experiments). The contour interval is 400 m using the dimensionalization STANDARD and negative values are dotted. The region within $r = 3L_R$, the outer boundary of the initial vortex, is shaded.

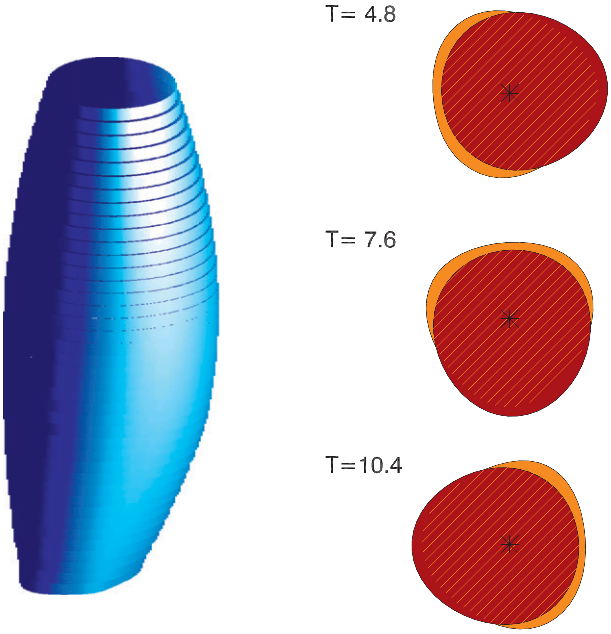

FIG. 4. An example of a steadily rotating vortex V state. The amplitude of projection of the leading $k = 1$ baroclinic mode is fixed at $|A_2^1| = 0.4405$. (left) A three-dimensional rendering of the vortex edge. (right) Three snapshots of cross sections through the vortex at $z = 2H$ (lower vortex, yellow) and $z = 4H$ (upper vortex, red).

frequency $\omega_{0(1,2)} \approx -0.0407$ to confirm the value from the linear theory calculation above (the estimated and theoretical values differ by approximately 2% because of discretization errors and the fitting process, with the estimate located in Fig. 5 where the curve intersects the vertical frequency axis) for the critical value of the rotation parameter $\Omega_c = \Omega - \omega_{0(1,2)}/k \approx -0.0843$. Further, the fitting parameters can be used to estimate $\omega_{2(1,2)}$ based on Eq. (28), giving $\omega_{2(1,2)} = -0.020$ (two significant figures). This calculated value of $\omega_{2(1,2)}$ will inform the calculations below.

c. *Modeled vortex response versus theoretical predictions*

Figure 6a shows the maximum wave activity $\max_t[\mathcal{A}(\Omega, M)]$, defined in Eq. (21) and normalized here by the angular impulse of the undisturbed vortex, recorded during the nonlinear model experiments. The critical value $\Omega = \Omega_c$ leading to linear resonant excitation of the $k = 1$ baroclinic mode [with vertical structure $Z_2^1(z)$] is marked with a dashed line. It is clear that the largest responses are for Ω near Ω_c, with a bias toward more positive values of Ω as M increases. There is an asymmetry in the response, as for fixed M the magnitude of the response increases slowly to a maximum as Ω increases, before decreasing relatively rapidly as Ω increases further. A weak secondary maximum in the response is present near $\Omega \approx -0.05$. Analysis of the linear problem shows that the $k = 2$ barotropic mode comes into resonance for $\Omega \approx -0.05$ [i.e., $\omega_{0(2,1)} \approx 0$]. The $k = 2$ barotropic mode is not forced directly in our model experiment, but it is significantly excited by nonlinearity associated with the fundamental mode. The secondary maximum is therefore most likely an example of a subharmonic resonance (see, e.g., Nayfeh and Mook 1979).

Figure 6b shows the maximum wave activity calculated from the weakly nonlinear predictions (29) and (23). Comparing Figs. 6a and 6b it is apparent that, in contrast to the single-layer vortex splitting experiments discussed in Part I, the amplitude Eq. (27) significantly overestimates the maximum wave activity in the nonlinear model experiments for Ω close to Ω_c. Hence the amplitude Eq. (27) does not lead to quantitatively successful prediction of the maximum wave activity in the nonlinear model experiments, although several qualitative features of Fig. 6a are captured nonetheless. These include the sense of the asymmetry in the response, the rapid decrease as Ω is increased past the value giving the maximum response, and the predicted amplitude of the response when $M \lesssim 0.1$. The fact that the amplitude Eq. (27) overpredicts the maximum amplitude attained by the disturbances to the vortex leads to the conclusion that

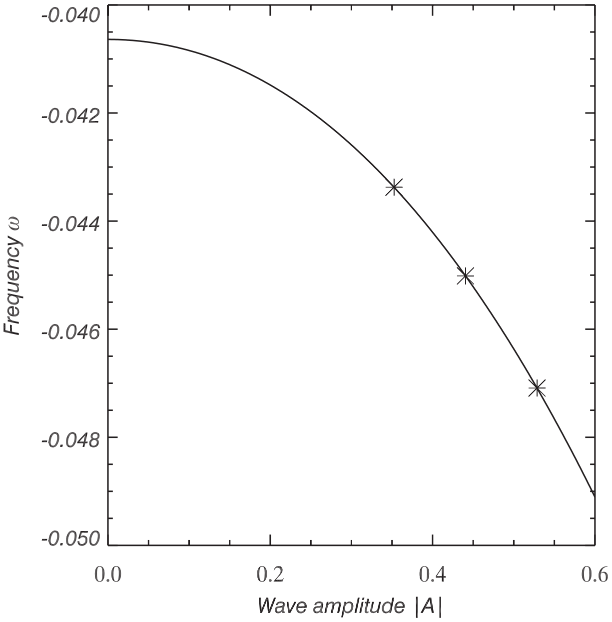

FIG. 5. Calculated frequencies of vortex V states in the full nonlinear model against the amplitude of the projection of vortex Rossby waves onto the leading baroclinic mode $|A_2^1|$.

some other nonlinear mechanism must act to limit the amplitude. At the present forcing amplitude ($M = 0.5$), the weakly nonlinear mechanism of quadratic correction to the Rossby wave phase speed is evidently too weak to be the dominant mechanism, otherwise Eq. (27) would be accurate. Next, the full nonlinear experiments will be investigated in more detail to discover more about the nature of the nonlinearity that does determine the limiting amplitude.

d. Vortex displacement SSWs in the model

To focus on model behavior resembling observed vortex displacement SSWs, a subset of the above experiments with $M = 0.375$ will be considered next. The relevant subset, for which the rotation parameter varies in the range $\Omega \in [-0.1, -0.05]$, is labeled as experiments (EXPTs) A–G in Fig. 6a. Figure 6a shows that the peak response in terms of wave activity $\mathcal{A}$ occurs for experiment D ($\Omega = -0.075$), which will be examined in detail first.

Figure 7 shows three-dimensional snapshot representations of the vortex edge (left panels) and cross sections (right panels) through the lower vortex ($z = 2H$, yellow) and upper vortex ($z = 4H$, red) during EXPT D. The times of the snapshots are selected to emphasize key stages in the vortex evolution. At early times the disturbance is well described by linear theory and the cylindrical initial condition (top panel) appears weakly perturbed. Filaments begin to be ejected from the central and lower vortex at around day 10, and the lower vortex in particular becomes increasingly distorted as can be seen at $t = 25.2$ days. From $t = 25.2$ to $t = 29.6$ days the disturbance to the vortex grows rapidly at all levels, and at upper levels the vortex becomes strained

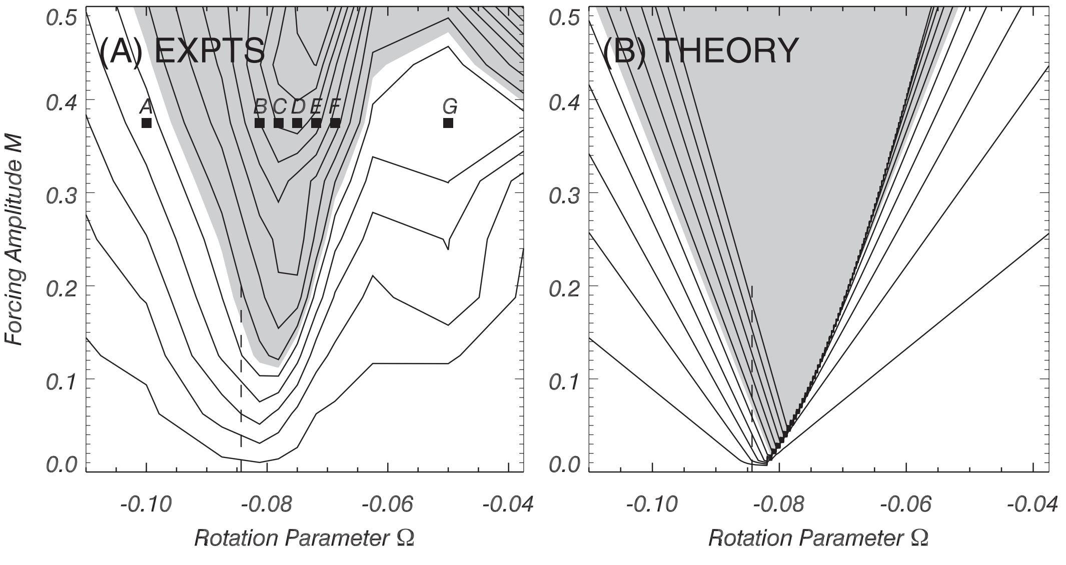

FIG. 6. (a) Maximum normalized wave activity [Eq. (21)], or excess angular impulse, during the first 40 days ($0 < \Delta_0 t/4\pi < 40$) as a function of (Ω, M) for the full nonlinear model experiments. The contour interval is 0.1 (starting at 0.05), values greater than 0.5 are shaded, and the dashed lines indicate the value of Ω leading to linear resonance in each case. (b) Maximum normalized wave activity as a function of (Ω, M) as predicted by Eq. (27). Contour values greater than 1 are suppressed. See text for details.

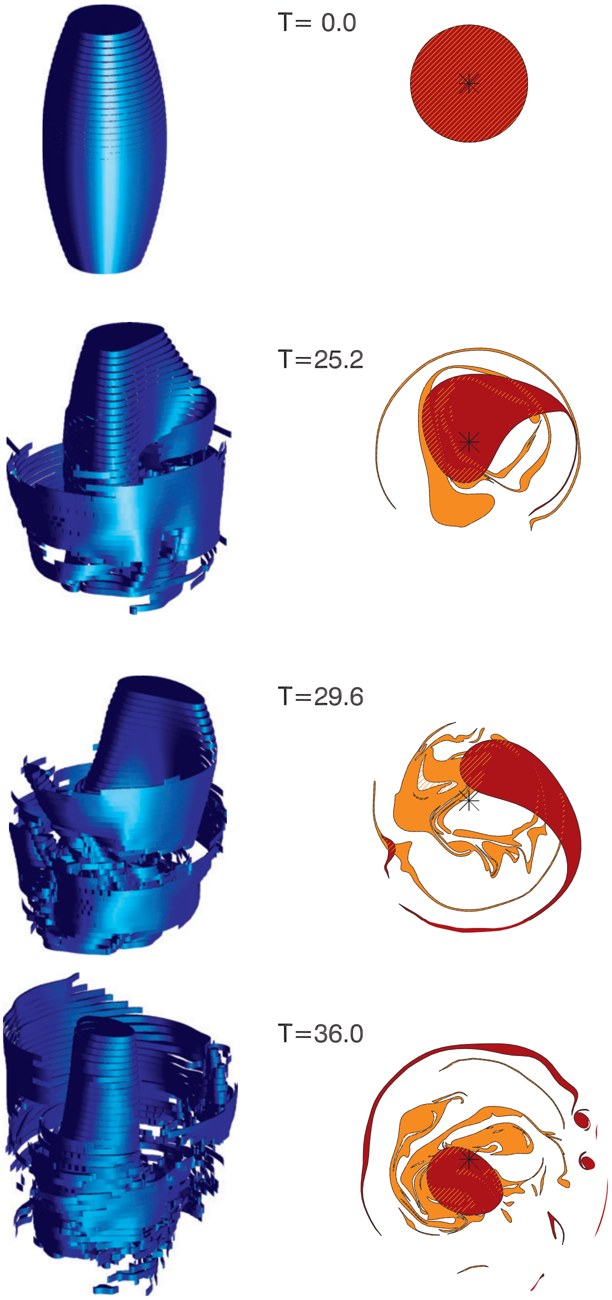

FIG. 7. (left) Snapshots of the three-dimensional vortex boundary at $t = 0, 25.2, 29.6$, and 36.0 days in EXPT D $(\Omega, M) = (-0.075, 0.375)$. For visualization purposes the figure is rotated 60° clockwise relative to the topography shown in Fig. 3. (right) Cross sections through the lower vortex ($z/H = 2$, yellow) and upper vortex ($z/H = 4$, red) at the same times.

out into the long "comma" shape characteristic of both composite and individual examples of observed displacement SSWs (e.g., Fig. 7 of Matthewman et al. 2009). Over the next 6 days disturbances to the vortex, which is by now significantly eroded, are seen to decay and by $t = 36$ days a significantly reduced vortex has reformed above the pole.

Figure 8 shows snapshots of the azimuthal mean wind $\overline{u}(r, z)$ during EXPT D, using the STANDARD dimensionalization. Note that because the background rotation is retrograde ($\Omega = -0.075$) the initial jet is weaker than that shown in Fig. 2a, and in fact closely resembles the observed midwinter jet structure and strength (e.g., Andrews et al. 1985, Fig. 1.4). As the experiment progresses the jet gradually weakens, particularly in the lower stratosphere where the zonal wind reverses, as can be seen by day 16. By day 25.2 the jet maximum is just over 30 m s^{-1}, compared with its peak of 65 m s^{-1} on day 0. Over the next four days the jet decelerates rapidly and disappears completely so that by day 29.2 the flow is easterly everywhere. The modeled evolution of the stratospheric jet therefore strongly resembles that during observed displacement SSWs, with a rapid reversal in jet strength over four model days.

The time evolution of $\overline{u}(R, z, t)$ during EXPT D is contrasted in Fig. 9 with that during EXPTs B and F ($\Omega = -0.08$ and $\Omega = -0.07$, respectively), where $R = 2.5L_R$ is a fixed radius close to the vortex edge. The change to the background rotation between EXPTs D, B, and F is small, equivalent to a velocity change of just ± 1.6 m s^{-1} at $r = R$, but nevertheless sufficient to significantly alter the response of both the vortex and the stratospheric jet. Unlike EXPT D, neither EXPT B nor EXPT F exhibit a rapid SSW-like deceleration of the stratospheric jet or a distortion to the vortex comparable in amplitude to that seen in Fig. 7 (day 29.2). The range of Ω producing an SSW-like response at $M = 0.375$ is clearly extremely narrow, again indicating the significance of resonance.

Figure 10 compares a snapshot of the vortex, as in Fig. 7, for EXPTs C, D, and E ($\Omega = -0.0775, -0.075$, and -0.0725, respectively) each of which does exhibit SSW-like behavior in the sense of an abrupt deceleration of the stratospheric jet. There are evidently significant differences between the three cases. In EXPT C the upper vortex remains relatively undisturbed throughout, while the lower vortex is strained out, partially mixed into the background, and then reforms. For EXPT D the amplitude of the displacements to the upper and lower vortex are seen to be roughly comparable, as discussed above. For EXPT E, it is the lower vortex that remains relatively unperturbed as the upper vortex is strained out and mixed. The nature of the nonlinear stage of the SSW-like behavior in the model therefore seems to depend extremely sensitively on exactly how close the linear first baroclinic mode is to resonance.

Figure 11 contrasts the time evolution of the baroclinic centroid $\mathbf{x}_{bc}(t)$, defined as

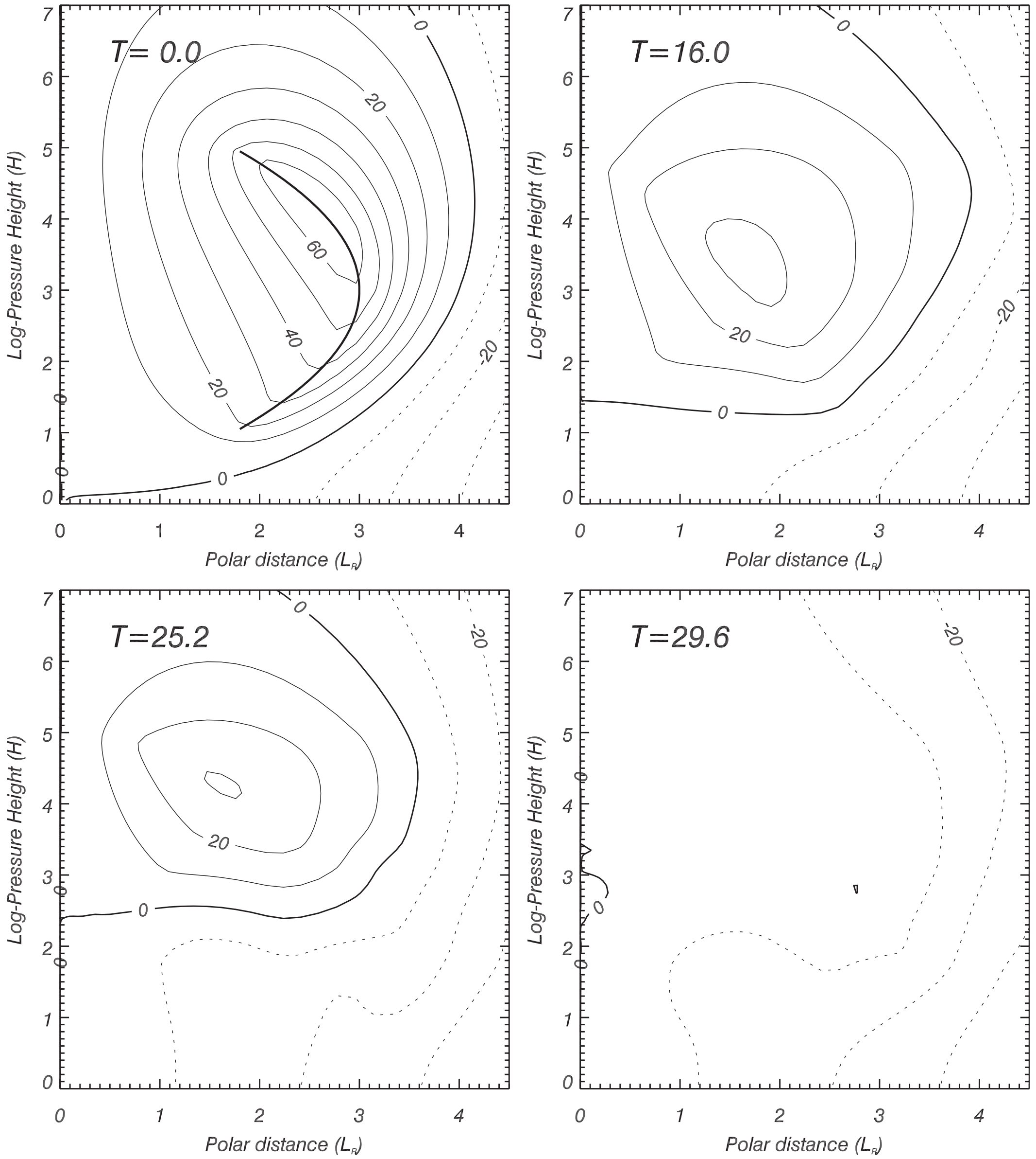

FIG. 8. Azimuthal mean wind $\overline{u}(r, z)$ in EXPT D $(\Omega, M) = (-0.075, 0.375)$ at times t = 0, 16, 25.2, and 29.6 days. The contour interval is 10 m s^{-1} under the dimensionalization STANDARD and negative contours are dotted. (top left) The initial vortex boundary.

$$\mathbf{x}_{\mathrm{bc}} = \frac{1}{\mathcal{M}}\int_{z_b}^{z_t} e^{-z} Z_2^1(z) \int_D \mathbf{x} q(\mathbf{x}, z, t)\, d\mathbf{x}\, dz, \qquad (33)$$

in EXPTs A–G. The baroclinic centroid measures the direction and amplitude of the vertical tilt of the vortex. For EXPT A ($\Omega = -0.1$) $\mathbf{x}_{\mathrm{bc}}(t)$ evolves in a closed clockwise (anticyclonic) orbit, consistent with near-linear and off-resonant excitation of vortex Rossby waves. Similarly, during EXPT G ($\Omega = -0.05$) the motion is anticlockwise/cyclonic, as here the excitation is off-resonant in the opposite sense. In the intermediate cases (C–F) the baroclinic centroid moves northward[4] in each case until the disturbance is large, nonlinear effects become important, and eventually either anticyclonic (C–E) or cyclonic (F) motion dominates. Hence, just as for the single-layer case examined in Part I, the resonant region of parameter space separates regimes of near-periodic anticyclonic and cyclonic oscillations. It is notable that

---

[4] Note that "north" in the model is defined with respect to the map of topographic forcing in Fig. 2.

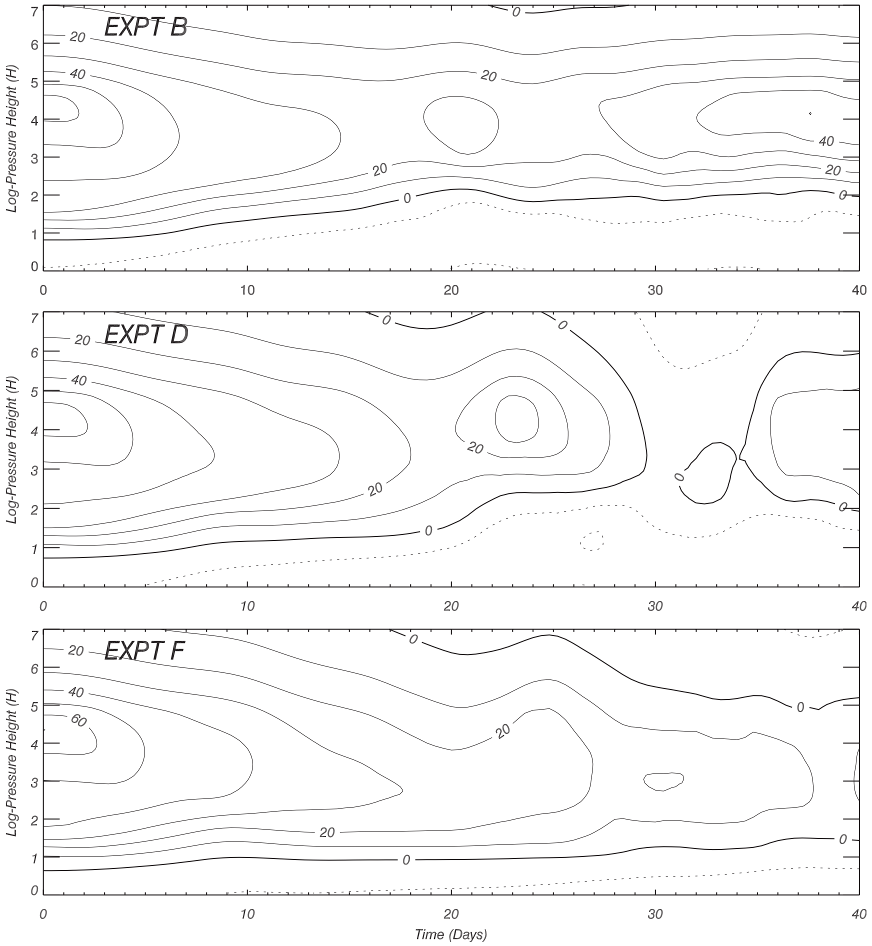

FIG. 9. Evolution in time and altitude of zonal (azimuthal) mean wind $\overline{u}(R, z, t)$ in EXPTs B $(\Omega, M) = (-0.08, 0.375)$, D $(\Omega, M) = (-0.075, 0.375)$, and F $(\Omega, M) = (-0.07, 0.375)$ at a fixed radius representative of the vortex edge ($R = 2.5L_R$). The contour interval is 10 m s^{-1} under the dimensionalization STANDARD and negative contours are dotted.

in EXPTs C–F there is little change in the rotation rate of the baroclinic centroid as the amplitude of the disturbance to the vortex grows, until the time when the maximum displacement of the centroid is reached. This is clear evidence that the quadratic correction to the Rossby wave phase speed has only a minor role in the dynamics, and the disturbance amplitudes are instead limited by the strongly nonlinear wave breaking that occurs at large amplitudes.

4. Conclusions

The main objective of this work was to explore the relationship between behavior resembling observed vortex displacement SSWs in a simple model and the predictions of linear and weakly nonlinear resonant excitation theory. In nature vortex displacement SSWs are baroclinic in their vertical structure (e.g., Matthewman et al. 2009), and the linear analysis performed here suggests that this is because the first baroclinic vortex Rossby wave mode is closest to linear resonant excitation by a general stationary wavenumber-1 forcing. This is in contrast to the vortex splitting SSWs modeled in Esler and Scott (2005) and Part I, where it is the wave-2 barotropic mode that is resonantly excited, again consistent with observations. To answer the first question posed in the introduction:

The results show clearly that to obtain a significant response at moderate forcing, the first baroclinic mode of the vortex must be excited near-resonantly by the forcing. Higher normal modes of the vortex, including the continuous spectrum, are not found to be significantly excited as the forcing velocity field $\mathbf{u}_M$ [defined in Eq. (24)] does not strongly project onto their vertical structure. A wide range of nonlinear behaviors can result from the linear excitation of the first baroclinic

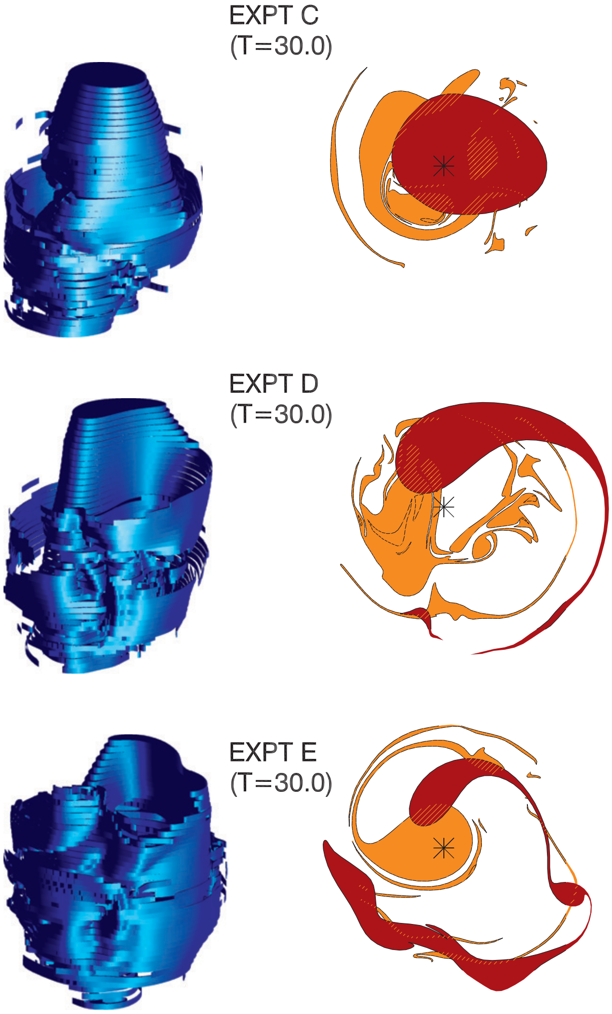

FIG. 10. Comparison of vortex structure at $t = 30$ days between EXPTs C $(\Omega, M) = (-0.0775, 0.375)$, D $(\Omega, M) = (-0.075, 0.375)$, and E $(\Omega, M) = (-0.0725, 0.375)$. (left) Three-dimensional snapshots of the entire vortex boundary; (right) cross sections through the lower vortex ($z/H = 2$, yellow) and upper vortex ($z/H = 4$, red).

mode, including both ‘‘top-down’’ and ‘‘bottom-up’’ breakdowns of the vortex. Top-down breakdowns are often reported as occurring in nature, especially during minor warming events, and are consistent with the explanation of descending critical layers given by Matsuno (1971).

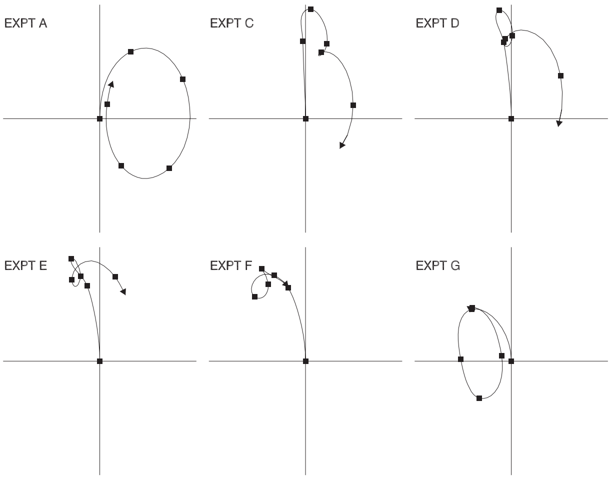

FIG. 11. Evolution of the vortex baroclinic centroid, defined in Eq. (33), in EXPTs A, C, D, E, F, and G. Days 0–21.2 are shown with squares plotted every 4 days.

It must be noted that even off-resonant forcing of the barotropic mode in our simple model can lead to significant departures of the entire vortex from the model pole, hence the use of the filtered topographic forcing used in our experiments. Since large barotropic departures from the pole are not typically observed, it can only be concluded that the polar vortices find equilibrium locations at which barotropic forcing is weak, or some other mechanism not present in the simple model acts to maintain their mean position.

It is evident that the nonlinear behavior of vortex displacement SSWs appears to be significantly more complicated than that of splitting SSWs [as reported in Esler and Scott (2005) and Part I], even within the present model. The nonlinear results and comparison with the linear and weakly nonlinear theory allow questions (i)–(iii) posed in the introduction to be answered as follows:

(i) For moderate forcings, the leading (quadratic in wave amplitude) nonlinear correction to the Rossby wave phase speed is insufficiently strong to act as the mechanism by which the amplitude of the fundamental vortex Rossby wave is limited. Unless the forcing amplitude is weak ($M \lesssim 0.1$), the growth of the fundamental wave follows the predictions of linear theory to a good approximation until an amplitude is reached at which high-order nonlinear effects become important. The vortex displacement SSWs can therefore be contrasted with the vortex splitting SSWs studied in Part I, for which a near-quadratic Rossby wave-phase speed correction was shown to be the dominant nonlinear mechanism.

(ii) The ‘‘nonlinear oscillator’’ amplitude Eq. (27) greatly overestimates equilibrium wave amplitudes close to resonance. However, Eq. (27) captures some qualitative features of the response, such as the peak response at finite forcing occurring for $\Omega > \Omega_c$, and the rapid decrease in peak response as Ω is increased further.

(iii) Strong nonlinearities, such as erosion of the vortex by wave breaking and ejection of filaments (see

> Figs. 7 and 10), must therefore act to cause the disturbances to the vortex to equilibrate at lower amplitudes than predicted under the quadratic phase speed correction mechanism. A plausible mechanism is that erosion of the vortex by ejection of filaments acts to alter its (effective) radial profile $R(z)$, and the changes to $R(z)$ lead to significant changes in the resonant frequency of the first baroclinic mode. The first baroclinic mode may thereby be brought out of resonance.

There remains the question of exactly how relevant the present model is for the situation in the winter stratosphere. Questions naturally arise as to the roles of neglected physics including inertia–gravity waves, more distributed vortex PV profiles (Scott et al. 2004), sensitivities to the structure of the lower boundary forcing including transient effects at tropopause level (Scinocca and Haynes 1998), relaxation of the quasigeostrophic approximation and spherical geometry (cf. Polvani and Saravanan 2000), the seasonal cycle, and the general state of the atmosphere elsewhere. The aim of future research will therefore be to establish the extent to which the nonlinear resonance mechanism identified here occurs in progressively more realistic models. Our view is that the present model captures the essential dynamics, but this view must be tested, starting with mechanistic models solving the primitive equations on a sphere and moving toward general circulation models used for direct numerical simulations of observed events.

Acknowledgments. NJM acknowledges support from a UK NERC studentship, and JGE from UK NERC Grant NE/G003122/1.

APPENDIX A

A Form of the Green's Function in an Anelastic Atmosphere

Here a form of the Green's function $G(|\mathbf{x} - \mathbf{x}'|, z|z')$ appearing in the streamfunction–PV relationship (7) is obtained. By definition the Green's function satisfies

$$\nabla_H^2 G + G_{zz} - G_z = \delta_2(\mathbf{x} - \mathbf{x}')\delta(z - z') \qquad \text{(A1)}$$

subject to the boundary conditions

$$G_z - \kappa G = 0 \quad \text{on} \quad z = 0, \quad G \to 0 \quad \text{as} \quad z \to \infty,$$

where $\delta(\cdot)$ and $\delta_2(\cdot)$ denote the Dirac delta function in one and two dimensions, respectively.

To solve Eq. (A1) for G, a hybrid sine-cosine Fourier transform is introduced as follows in order to separate the vertical problem. Consider first the Sturm–Liouville problem defined by

$$\frac{d^2 Z}{dz^2} - \frac{dZ}{dz} + \gamma^2 Z = 0,$$
$$\frac{dZ}{dz} - \kappa Z = 0 \quad \text{on} \quad z = 0, D.$$

This is an eigenvalue problem in γ, and Sturm–Liouville theory dictates that there is a discrete unbounded infinite sequence of real eigenvalues $\{\gamma_j\}$, with associated eigenfunctions $Z_j(z)$. These can be calculated as

$$\begin{aligned} \gamma_0 &= \sqrt{\kappa(1 - \kappa)}, \\ Z_0(z) &= e^{\kappa z}, \\ \gamma_j &= \sqrt{\frac{1}{4} + \frac{j^2\pi^2}{D^2}}, \\ Z_j(z) &= e^{z/2}\cos\left[\frac{j\pi z}{D} + \epsilon(j)\right], \quad (j \geq 1) \end{aligned}$$

where

$$\tan\epsilon(j) = \frac{D(1 - 2\kappa)}{2j\pi}.$$

Sturm–Liouville theory allows any function $f(z)$ on $[0, D]$ to be expanded in a generalized Fourier series as

$$f(z) = \sum_{j=0}^{\infty} \frac{\langle f, Z_j\rangle}{\langle Z_j, Z_j\rangle} Z_j(z),$$

where the inner product $\langle\cdot,\cdot\rangle$ is defined for functions $f(z)$, $g(z)$ to be

$$\langle f, g\rangle = \int_0^D e^{-z} f(z) g(z)\, dz.$$

It is straightforward to calculate

$$\langle Z_0, Z_0\rangle = \frac{1 - e^{-(1-2\kappa)D}}{1 - 2\kappa}, \quad \langle Z_j, Z_j\rangle = \frac{D}{2},$$

leading to the relation

$$f(z) = \frac{1 - 2\kappa}{1 - e^{-(1-2\kappa)D}}\left[\int_0^D e^{-(1-\kappa)\overline{z}} f(\overline{z})\, d\overline{z}\right] e^{\kappa z} + \sum_{j=1}^{\infty}\left\{\frac{2}{D}\int_0^D f(\overline{z}) e^{-\overline{z}/2} \cos\left[\frac{j\pi\overline{z}}{D} + \epsilon(j)\right] d\overline{z}\right\} e^{z/2} \cos\left[\frac{j\pi z}{D} + \epsilon(j)\right].$$

Introducing $m = \pi j/D$, the limit $D \to \infty$ may now be taken. Using the standard definition of a Riemann integral on $[0, \infty)$, the relation above becomes the transform pair

$$
\begin{aligned}
f(z) &= \hat{f}_H^0 e^{\kappa z} + \sqrt{\frac{2}{\pi}}\int_0^\infty \hat{f}_H(m) e^{z/2}\cos[mz + \vartheta(m)]\,dm,\\
\hat{f}_H^0 &= (1 - 2\kappa)\int_0^\infty f(z) e^{-(1-\kappa)z}\,dz,\\
\hat{f}_H(m) &= \sqrt{\frac{2}{\pi}}\int_0^\infty f(z) e^{-z/2}\cos[mz + \vartheta(m)]\,dz,
\end{aligned}
$$

where

$$\tan\vartheta(m) = \frac{1 - 2\kappa}{2m}.$$

Applying the forward transform to Eq, (A1) results in

$$
\begin{aligned}
&\nabla_H^2 \hat{G}_H^0 - \kappa(1 - \kappa)\hat{G}_H^0 = (1 - 2\kappa)e^{-(1-\kappa)z'}\delta_2(\mathbf{x}),\\
&\nabla_H^2 \hat{G}_H - \left(m^2 + \frac{1}{4}\right)\hat{G}_H\\
&\quad = \sqrt{\frac{2}{\pi}} e^{-z'/2}\cos[mz' + \vartheta(m)]\delta_2(\mathbf{x}),
\end{aligned}
$$

which can be solved to give

$$
\begin{aligned}
\hat{G}_H^0(r) &= \frac{1}{2\pi}(1 - 2\kappa)e^{-(1-\kappa)z'}K_0[\sqrt{\kappa(1-\kappa)}r],\\
\hat{G}_H(r,m) &= \frac{1}{\sqrt{2}\pi^{3/2}}e^{-z'/2}\cos[mz' + \vartheta(m)]K_0\left(\sqrt{m^2 + \frac{1}{4}}r\right),
\end{aligned}
$$

where $K_0(\cdot)$ is a modified Bessel function of the second kind. Inserting into the inverse transform yields the result

$$
\begin{aligned}
G(r, z|z') = {}& \frac{1}{2\pi}(1 - 2\kappa)e^{\kappa z-(1-\kappa)z'}K_0[\sqrt{\kappa(1-\kappa)}r]\\
&+ \frac{1}{\pi^2}e^{(z-z')/2}\int_0^\infty \cos[mz' + \vartheta(m)]\cos[mz + \vartheta(m)]K_0\left(\sqrt{m^2 + \frac{1}{4}}r\right)dm,
\end{aligned}
\tag{A2}
$$

which gives the form of the Green's function used in section 2b above.

APPENDIX B

Calculation of Vortex V States

Here the method of calculation of the steadily rotating vortex V states described in section 3b is reported. The standard V-state algorithm (Wu et al. 1984) was found not to converge in conjunction with CASL. The problem relates to the underlying grid used to obtain the velocity $\mathbf{u}$ from the vortex edge position $\eta(\theta, z)$. Unlike for standard contour dynamics, the presence of the grid ensures that the functional $\mathbf{u}[\eta]$ within CASL does not vary sufficiently smoothly with η for the purposes of the algorithm.

Hence a new algorithm, based on a modal decomposition of the disturbance, is described next. The new algorithm is not intended as an improvement on that of Wu et al. (1984), but rather as a technical fix to overcome as far as possible the grid problem associated with CASL. In fact the problem is only partially alleviated, and the calculated states described in section 3b remain approximate. Furthermore, solutions are found only for V states close to linear normal modes. The aim of the new algorithm is to make reasonable estimates for $\omega_{2(k,j)}$ as described in section 3b.

First, the disturbance to the vortex edge is expanded in terms of its linear eigenfunctions, where the system is treated as being fully discretized such that the continuous spectrum can be treated in the same manner as the normal modes from the outset:

$$\eta(\theta, z) = \mathrm{Re}\sum_{k=1}^{K}\sum_{j=1}^{J} A_j^k Z_j^k(z)\exp ik\theta. \tag{B1}$$

The amplitude of a single mode ($j = j^*$, $k = k^*$), namely the fundamental, is fixed as $A_{j^*}^{k^*} = a$. The aim of the algorithm is then to find the $JK \times JK$ unknowns $[\omega; A_j^k; j = 1, J; k = 1, K; (j, k) \neq (j^*, k^*)]$ consistent with a solution that is steadily rotating with angular frequency ω. For a given set of coefficients A_j^k the CASL algorithm can be used to obtain the velocity on the vortex edge everywhere:

$$(\mathbf{u}\cdot\mathbf{n})_c = \mathrm{Re}\sum_{k=1}^{K}\sum_{j=1}^{J} iU_j^k(\mathbf{A})Z_j^k(z)\exp ik\theta,$$

where $\mathbf{A}$ is a vector with JK components $\{A_j^k\}$. Inserting into Eq. (9), and seeking a solution that is steadily propagating with ω, the system of JK nonlinear equations to be solved is

$$
\begin{aligned}
&(\omega - \Omega k)A_j^k = U_j^k(\mathbf{A}) \quad j = 1,J \quad k = 1,K \\
&\quad (j,k) \neq (j^*,k^*), \quad (\omega - \Omega k^*)a = U_{j^*}^{k^*}(\mathbf{A}). \qquad \text{(B2)}
\end{aligned}
$$

The system (B2) is solved numerically using a damped fixed point iteration, with the numerical eigenvalues $\omega_{0(k,j)}$ found for the linear problem used to improve the update formulas as follows:

$$
\begin{aligned}
F_j^{k,(n)} &= \frac{U_j^k[\mathbf{A}^{(n)}] - \omega_{0(k,j)}}{\omega^{(n)} - \omega_{0(k,j)}}, \\
A_j^{k,(n+1)} &= \gamma A_j^{k,(n)} + (1-\gamma)F_j^{k,(n)}, \\
\omega^{(n+1)} &= \Omega k^* + \frac{1}{a}U_{j^*}^{k^*}[\mathbf{A}^{(n)}], \qquad \text{(B3)}
\end{aligned}
$$

where the superscripts (n) refer to the nth estimate of ω and $\{A_j^k\}$. The initial guesses are taken to be zero, and γ is a damping parameter for the iteration. A value of $\gamma = 0.5$ facilitated convergence for the solutions shown in section 3b. The iteration is continued until successive guesses converge to within a predetermined tolerance: $|A_j^{k,(n+1)} - A_j^{k,(n)}| < \delta = 10^{-5}$.

The results of section 3b are constructed from a small subset of modes $J = K = 4$, as tests revealed that the given estimate of $\omega_{2(1,2)}$ is relatively insensitive to the inclusion of higher harmonics. Calculated V states are tested by integrations of the nonlinear model in order to ensure that a steadily rotating state has indeed been found (see Fig. 4).

REFERENCES

Andrews, D. G., J. R. Holton, and C. B. Leovy, 1985: *Middle Atmosphere Dynamics*. Academic Press, 489 pp.

Charlton, A. J., and L. M. Polvani, 2007: A new look at stratospheric sudden warmings. Part I: Climatology and modeling benchmarks. *J. Climate,* **20,** 449–469.

Dritschel, D. G., and R. Saravanan, 1994: Three-dimensional quasi-geostrophic contour dynamics, with an application to stratospheric vortex dynamics. *Quart. J. Roy. Meteor. Soc.,* **120,** 1267–1297.

——, and M. P. Ambaum, 1997: A contour-advective semi-Lagrangian algorithm for simulating fine-scale conservative dynamical fields. *Quart. J. Roy. Meteor. Soc.,* **123,** 1097–1130.

Esler, J. G., and R. K. Scott, 2005: Excitation of transient Rossby waves on the stratospheric polar vortex and the barotropic sudden warming. *J. Atmos. Sci.,* **62,** 3661–3682.

——, L. M. Polvani, and R. K. Scott, 2006: The Antarctic sudden stratospheric warming of 2002: A self-tuned resonance? *Geophys. Res. Lett.,* **33,** L12804, doi:10.1029/2006GL026034.

Held, I. M., R. T. Pierrehumbert, S. T. Garner, and K. L. Swanson, 1995: Surface quasi-geostrophic dynamics. *J. Fluid Mech.,* **282,** 1–20.

Macaskill, C., W. E. P. Padden, and D. G. Dritschel, 2003: The CASL algorithm for quasi-geostrophic flow in a cylinder. *J. Comput. Phys.,* **188,** 232–251.

Matsuno, T., 1971: A dynamical model of the stratospheric sudden warming. *J. Atmos. Sci.,* **28,** 1479–1494.

Matthewman, N. J., and J. G. Esler, 2011: Stratospheric sudden warmings as self-tuning resonances. Part I: Vortex splitting events. *J. Atmos. Sci.,* **68,** 2481–2504.

——, ——, A. J. Charlton-Perez, and L. M. Polvani, 2009: A new look at stratospheric sudden warmings. Part III: Polar vortex evolution and vertical structure. *J. Climate,* **22,** 1566–1585.

Nayfeh, A. H., and D. T. Mook, 1979: *Nonlinear Oscillations*. Wiley, 704 pp.

Pedlosky, J., 1987: *Geophysical Fluid Dynamics*. 2nd ed. Springer-Verlag, 710 pp.

Plumb, R. A., 1981: Instability of the distorted polar night vortex: A theory of stratospheric warmings. *J. Atmos. Sci.,* **38,** 2514–2531.

Polvani, L. M., and R. Saravanan, 2000: The three-dimensional structure of breaking Rossby waves in the polar wintertime stratosphere. *J. Atmos. Sci.,* **57,** 3663–3685.

——, N. J. Zabusky, and G. R. Flierl, 1989: Two-layer geostrophic vortex dynamics. Part 1. Upper-layer V-states and merger. *J. Fluid Mech.,* **205,** 215–242.

Porter, D., and D. S. G. Stirling, 1990: *Integral Equations: A Practical Treatment, from Spectral Theory to Applications*. Cambridge University Press, 372 pp.

Scinocca, J. F., and P. H. Haynes, 1998: Dynamical forcing of stratospheric planetary waves by tropospheric baroclinic eddies. *J. Atmos. Sci.,* **55,** 2361–2392.

Scott, R. K., and D. G. Dritschel, 2005: Quasi-geostrophic vortices in compressible atmospheres. *J. Fluid Mech.,* **530,** 305–325.

——, ——, L. M. Polvani, and D. W. Waugh, 2004: Enhancement of Rossby wave breaking by steep potential vorticity gradients in the winter stratosphere. *J. Atmos. Sci.,* **61,** 904–918.

Smith, A. K., 1989: An investigation of resonant waves in a numerical model of an observed sudden stratospheric warming. *J. Atmos. Sci.,* **47,** 3038–3054.

Tung, K. K., and R. S. Lindzen, 1979: A theory of stationary long waves. Part I: A simple theory of blocking. *Mon. Wea. Rev.,* **107,** 714–734.

Wang, X., and J. Fyfe, 2000: Onset of edge wave breaking in an idealized model of the polar stratospheric vortex. *J. Atmos. Sci.,* **57,** 956–966.

Watson, G. N., 1944: *A Treatise on the Theory of Bessel Functions*. 2nd ed. Cambridge University Press, 804 pp.

Waugh, D. W., and D. G. Dritschel, 1999: The dependence of Rossby wave breaking on the vertical structure of the polar vortex. *J. Atmos. Sci.,* **56,** 2359–2375.

——, and W. J. Randel, 1999: Climatology of Arctic and Antarctic polar vortices using elliptic diagnostics. *J. Atmos. Sci.,* **56,** 1594–1613.

Wu, H. M., E. A. Overman, and N. J. Zabusky, 1984: Steady state solutions of the Euler equations in two dimensions: Rotating and translating V-states with limiting cases. I. Numerical algorithms and results. *J. Comput. Phys.,* **53,** 42–71.